RESEARCH ARTICLE

Macromolecular Chemistry and Physics
www.mcp-journal.de

Oxides and Nitrides with Asymmetric Pore Structure from Block Copolymer Co-Assembly and Non-Solvent Induced Phase Separation

*Sarah A. Hesse, Kevin E. Fritz, Peter A. Beaucage, Ethan M. Susca, Jin Suntivich, and Ulrich Wiesner**

Materials combining an asymmetric pore structure with mesopores everywhere enable high surface area accessibility and fast transport, making them attractive for e.g., energy conversion and storage applications. Block copolymer (BCP)/inorganic precursor co-assembly combined with non-solvent induced phase separation (NIPS) provides a route to materials in which a mesoporous top surface layer merges into an asymmetric support with graded porosity along the film normal and mesopores throughout. Here, the co-assembly and non-solvent-induced phase separation (CNIPS) of poly(isoprene)-*b*-poly(styrene)-*b*-poly(4-vinylpyridine) (ISV) triblock terpolymer and titanium dioxide (TiO_2) sol-gel nanoparticlesare reported. Heat-treatment in air results in free-standing asymmetric porous TiO_2. Further thermal processing in ammonia results in free-standing asymmetric porous titanium nitride (TiN). processing changes alter structural membrane characteristics is demonstrated. Changing the CNIPS evaporation time results in various membrane cross-sections (finger-like to sponge-like). Oxide and nitride material composition, crystallinity, and porosity are tuned by varying thermal processing conditions. Finally, thermal processing condition effects are probed on phase-pure asymmetric nitride membrane behavior using cyclic voltammetry to elucidate their influence, e.g., on specific capacitance. Results provide further insights into improving asymmetric and porous materials for applications including energy conversion and storage, separation, and catalysis and motivate a further expansion of CNIPS to other (in)organic materials.

1. Introduction

When designing electrodes for energy conversion and storage applications, high power density and high energy density are desirable.[1,2] For electrochemical double-layer capacitors (EDLCs) utilizing high-surface-area porous materials, there exists an inherent tradeoff between the two at fast charge/discharge rates, as only a small pore fraction is accessible due to the limited mass transport into and out of the electrodes, leading to pore underutilization. Reducing electrode thickness can improve pore utilization, but at the expense of energy density.

Mesoporous materials have contributed to the ability to overcome this inherent energy and power density tradeoff.[3–9] Block copolymer (BCP) self-assembly (SA) is a highly versatile and controllable route to obtaining mesoporous materials, as BCPs can be used to structure-direct a wide range of organic or inorganic materials.[10] Further processing to remove the polymer results in periodically ordered mesoporous inorganic materials which have homogeneous pore sizes typically on the order of tens of nanometers throughout the material.[11–13]

S. A. Hesse[+], K. E. Fritz, P. A. Beaucage[++], E. M. Susca, J. Suntivich, U. Wiesner
Department of Materials Science and Engineering
Cornell University
Ithaca, NY 14853, USA
E-mail: ubw1@cornell.edu

The ORCID identification number(s) for the author(s) of this article can be found under https://doi.org/10.1002/macp.202200304

[+]Present address: SLAC National Accelerator Laboratory, Menlo Park, CA 94025, USA

[++]Present address: NIST Center for Neutron Research, National Institute of Standards and Technology, Gaithersburg, MD 20899, USA

DOI: 10.1002/macp.202200304

S. A. Hesse[+]
Department of Chemistry and Chemical Biology
Cornell University
Ithaca, NY 14853, USA

U. Wiesner
Kavli Institute at Cornell for Nanoscale Science
Cornell University
Ithaca, NY 14853, USA

These structures generally represent equilibrium mesophase morphologies and can have high surface areas thus improving energy densities.[12,14] Yet at fast charge/discharge rates, the power density plateaus and the energy density drops due to the limited mass transport rate into and out of the mesoporous material.[15]

To overcome these limitations, it is desirable to create materials with increased pore accessibility to enhance power density at fast charge/discharge rates, while retaining high energy density. The self-assembly and non-solvent-induced phase separation (SNIPS) process combines BCP SA with an industrially scalable process called non-solvent-induced phase separation (NIPS).[16–18] As solvents evaporate during SNIPS, BCP SA is not allowed to reach equilibrium. Rather, the structure is kinetically trapped in an asymmetric state along the film normal due to quenching in a non-solvent bath duringNIPS. The resulting porous membranes possess a mesoporous top surface separation layer that merges into an asymmetric macroporous support structure. The mesoporous top separation layer can be tuned to possess a highly periodically ordered array of homogeneously sized pores, thus enabling high selectivity in separation applications.[19] The macroporous support structure is tunable and contributes to the mechanical stability of the membranes.[20] As a result of the high pore density and small thickness of order 100 nm of the mesoporous separation layer atop the macroporous support, highly permeable ultrafiltration membranes also enable high flux.[21] While initially restricted to organic materials, the SNIPS process was expanded to co-assembly and non-solvent-induced phase separation (co-assembly and NIPS = CNIPS) providing access to both organic-inorganic hybrid and inorganic functional materials.[22] During CNIPS, BCPs are used to structure-direct either organic or inorganic additives (the former may subsequently be converted into inorganic materials), hence co-assembly, into kinetically trapped asymmetric membrane structures.[22,23]

Additives that have been introduced include, amongst others, phenol formaldehyde resols as carbon precursors or titanium dioxide (TiO_2) sol gel-derived nanoparticles (NPs). By introducing a substantial amount of organic or inorganic additives in the CNIPS process, the resulting organic/organic or organic/inorganic hybrids can be further heat-processed to obtain carbons or oxides and nitrides, respectively.[15,22–24] Carbons are the material of choice, for example, for lithium-ion batteries, while titanium nitride (TiN) is stable to higher voltages, thus making it a desirable support material in electrocatalysis.[12,25] While these materials classes can themselves already find a range of applications, as we showed for the first time very recently the combination of asymmetric, hierarchical pore structure with well-defined mesoporosity throughout the materials enables improved performance with respect to both power and energy density, in particular at fast charge/discharge rates.[15] This approach overcomes the inherent trade-off between high-surface-area and high-flux requirements discussed earlier that had limited the performance of porous materials with other architectures. The resulting asymmetric materials typically have similar specific surface areas as compared to their mesoporous counterparts; However, this high surface area as a result of the mesopores throughout the membranes is more accessible due to the superimposed pore hierarchy including graded macropores, allowing for rapid ion diffusion into and out of the material, for example, resulting in record-setting power densities at high energy densities in EDLCs.[15]

While this original report described record-setting carbon as well as titanium nitride materials and their electrochemical characterization, it did not provide a comprehensive account of the correlation of SNIPS and thermal processing parameters with porous materials structure. This original work was therefore more recently followed up with an in-depth study of these correlations for carbon materials.[24] The focus of this present report is to do the same for the nitride materials. We will provide fundamental insights into the synthesis of asymmetric, hierarchically porous TiO_2 and TiN membranes with mesopores throughout the materials resulting from a combination of triblock terpolymer-based CNIPS with subsequent heat-processing steps. It is the triblock terpolymer SA-derived mesopores throughout these membranes that sets these materials apart from other electrode materials with hierarchical pore structure, including asymmetric carbons derived from NIPS.[26–28] We demonstrate how careful control of various processing parameters, for example, solvent evaporation time and maximum processing temperature, enable tuning of final membrane properties, including variations in membrane substructure and changes in degree of crystallinity, from mixed phase to single phase inorganic materials, respectively. Finally, cyclic voltammetry (CV) was used on each of the resulting phase-pure asymmetric nitrides to study the effects of thermal processing on their capacitive performance.

2. Experimental Section

2.1. Materials

2.1.1. Materials

Unless otherwise stated, materials were used in the form they were received. 1,4-dioxane (DOX, Sigma-Aldrich, anhydrous, 99.8%) and tetrahydrofuran (THF, Sigma-Aldrich, anhydrous, ≥99.9%, inhibitor-free) were used to prepare casting solutions. TiO_2 sol NPs were prepared using hydrochloric acid (HCl, VWR, BDH, ACS Grade, 36.5–38%), titanium tetraisopropoxide (TTIP, Sigma Aldrich, 99.999% trace metals basis or Alfa Aesar, 99.995% metals basis), and THF (Sigma-Aldrich, anhydrous, ≥99.9%, inhibitor-free). During SNIPS syntheses, deionized (DI) water with a resistivity of 18.2 MΩcm was used as non-solvent in the precipitation bath.

Heat-processing was performed using the following gases: Either ammonia (NH_3) from Airgas, (anhydrous, 99.9%, purified over a SAES MicroTorr MC400-702F purifier to remove residual moisture/oxygen) or from Praxair, (electronic grade, 99.9999%) for the nitride synthesis; Argon (Ar, Airgas, high purity) or nitrogen (N_2, Airgas, high purity) to purge the furnace tube of residual NH_3.

The following chemicals were used in the electrochemical measurements: perchloric acid ($HClO_4$, GFS Chemicals, Veritas double-distilled), Pelco Colloidal Gold Paste (Ted Pella), Omegabond 101 epoxy (Omega Engineering), argon (Ar, Airgas,

ultra-high purity), and deionized water (DI water) with a resistivity of 18.2 MΩcm.

2.2. Materials Synthesis/Preparation

2.2.1. Polymer Synthesis and Characterization

A previously described sequential living anionic polymerization process was employed to synthesize the poly(isoprene)-*b*-poly(styrene)-*b*-poly(4-vinylpyridine) (ISV) triblock terpolymer.[17] The ISV triblock terpolymer used in this study had a total molar mass of 113 kg mol^{-1}. The volume fractions for poly(isoprene) (PI), poly(styrene) (PS), and poly(4-vinylpyridine) (P4VP) were 29 vol%, 59 vol%, and 12 vol%, respectively. The ISV polydispersity index (PDI) was 1.3 determined via gel permeation chromatography (GPC). Using a combination of GPC and ^{1}H nuclear magnetic resonance spectroscopy (^{1}H NMR), the molar mass of the individual blocks and entire BCP were determined based on the molar mass of the PI block obtained from GPC (using PI standards) on an aliquot of PI extracted during synthesis. For block fraction analysis, the polymer was dissolved in chloroform-d (D, 99.8%, Cambridge Isotope Laboratories) and measured using a Varian INOVA 400 MHz ^{1}H solution NMR spectrometer. For ISV polydispersity determination against PS standards, ISV was dissolved in THF and analyzed using a Waters ambient-temperature GPC equipped with a Waters 410 differential refractive index (RI) detector (flow-rate 1 mL min^{-1}).

2.2.2. Casting Solutions

The casting solutions were prepared by first dissolving ISV at 15 wt.% concentration in a 7:3 (by weight) solvent mixture of DOX:THF. Typically, 0.1 g of ISV was used to prepare the initial solution of ISV in 7:3 DOX:THF. The solution was stirred until it appeared homogeneous. The TiO_2 sol was prepared in a separate vial via a hydrolytic sol-gel route, adapted from a previously reported process.[25,29–31] 1.0 mL TTIP was added to 0.3 mL HCl in a vial with septum and stirred vigorously for 5 min. After that time, 2 mL of THF was added. The mixture was again stirred for 2 min before being added to the casting solution. 7.9 vol% ISV+TiO_2 was the volume percent of the casting solution.

2.2.3. Casting

The asymmetric materials were prepared via a process called S/CNIPS. In this process, the casting solution was pipetted onto a glass substrate. Thereafter, a doctor blade was used to hand cast a thick film of predetermined height. Prior to casting, the gate height (height between the casting blade and substrate) was adjusted to 305 to 381 μm thickness using feeler blades. After casting, the solvents in the film were allowed to evaporate for a specified amount of time (typically 75 s unless otherwise stated) to allow for a concentration gradient to form along the film normal. After this evaporation period, the films were plunged into a non-solvent DI water bath. This step precipitated the ISV+TiO_2, thereby turning the concentration gradient into a structural gradient.

2.2.4. Thermal Processing

Once the membranes were prepared, they were dried in a vacuum oven and then heated first to 50 °C for 2 h, followed by an additional heating step for 5 h at 130 °C. Thereafter, a flow furnace was used for further heat-processing steps. In order to produce an oxide material, the furnace was kept open to air. The temperature profile for this step was 1 °C min^{-1} to final temperatures of 300, 400, or 500 °C, respectively. The final temperatures of 300, 400, or 500 °C were held for 3 h before samples were allowed to cool back to room temperature (RT) at ambient rate. In order to produce free-standing nitrides, either the oxide materials or the original 130 °C hybrid materials were heated in a flow furnace under flowing NH_3 gas (10 liter h^{-1}). Regardless of oxides or hybrids being used for making the nitrides, the temperature profile was 5 °C min^{-1} to 600 °C. The temperature was then held at 600 °C for 6 h before being allowed to cool to RT at ambient rate. Before removing the sample from the furnace, the tube was purged with either Ar or N_2 in order to remove any remaining NH_3 gas. In the case of the anatase to rutile series (Figure 6), the ramp rate was 1 °C min^{-1} to 500, 700, 825, and 875 °C with a dwell time of 0.1 h instead of 3 h. To that end, samples were treated in a flow furnace that was open to air.

2.3. Materials Characterization

2.3.1. SEM Analysis

Scanning electron microscopy (SEM) micrographs were obtained using either a TESCAN MIRA3 FE-SEM (in-lens detector, accelerating voltage of 5–15 kV) or a ZEISS Gemini 500 SEM (accelerating voltage of 2 kV). The samples were either left uncoated or were coated with gold-palladium prior to imaging using a Denton Vacuum Desk II. Some of the SEM images were brightness/contrast adjusted.

2.3.2. X-Ray Diffraction

X-ray diffraction (XRD) data for hybrids, oxides, and nitrides were collected on a Rigaku Ultima IV diffractometer equipped with a D/teX Ultra detector using CuKα radiation (40 V, 44 mA, $\lambda = 1.54$ Å) and a step size of 0.02° (2theta) at 1° min^{-1}. MDI Jade was used for the analysis by fitting the peak profiles.

Lattice parameters for TiN were calculated using the raw XRD data using the (200) reflection. The coherent scattering domain sizes were calculated using the Debye–Scherrer analysis with shape factor k = 1, and were the result of an average of the values for the first five peaks, unless otherwise noted. Peak markings correspond to the expected peak positions and relative intensities of cubic $Fm\bar{3}m$ (space group #225) TiN (osbornite; ICSD entry #00-038-1420) with a reported lattice parameter of 4.2417 Å.

Lattice parameters for the anatase TiO_2 were calculated using the raw XRD data of the (200) and (105) reflections. The coherent scattering domain sizes were calculated using the Debye–Scherrer analysis with a shape factor k = 1, and were the result of the values obtained using the (101), (200), (105), and (211) reflections, unless otherwise noted. Peak markings correspond to

the expected peak positions and relative intensities of a tetragonal crystal system of $I4_1/amd$ (space group #141) for anatase TiO_2 (ICSD entry #01-070-7348) with a reported lattice parameter of a = b = 3.7840 Å and c = 9.5000 Å.

Lattice parameters for rutile TiO_2 were calculated using the raw XRD data of the (101) and (111) reflections. The coherent scattering domain sizes were calculated using the Debye–Scherrer analysis with a shape factor of k = 1, and were the result of the values obtained using the (110), (101), (200), (111), (210), (211), and (220) reflections. Peak markings correspond to the expected peak positions and relative intensities of a tetragonal crystal system of $P4_2/mnm$ (space group #136) for rutile TiO_2 (ICSD entry #00-021-1276) with a lattice parameter of a = b = 4.5933 Å and c = 2.9592 Å.

These analyses represent the lower limit of the domain sizes as instrumental and other sources of peak broadening were not accounted for.

2.3.3. Nitrogen Sorption

Nitrogen adsorption-desorption isotherms were recorded using a Micromeritics ASAP 2020 surface area and porosity analyzer at −196 °C. The Brunauer–Emmett–Teller (BET) method was used to obtain the specific surface areas of the various oxides and nitrides.[32,33] Pore size distributions were obtained using the Barrett–Joyner–Halenda (BJH) analysis.[34] Reported errors in surface area were a result of the standard deviations of repeated sample weighing. The standard deviation of the full-width at half-maximum (FWHM) was a result of fitting the pore size distribution with a least-squares fit using a gaussian function in Igor Pro.

2.3.4. Thermogravimetry Analysis

A TA Instruments Q500 thermogravimetric analyzer (TGA) was used for thermogravimetric measurements. The temperature was ramped from RT at 1 °C min^{-1} to 300, 400, or 500 °C, respectively, for each of the three samples measured. There the temperature was held isothermally for 3 h before being allowed to cool back to RT at ambient rate. The samples were processed in air.

2.3.5. Electrochemical Measurements

Electrodes were fabricated by adhering titanium wire to the nitride monoliths using a two-step procedure. First, the wires were affixed to the monoliths with conductive gold paint and allowed to cure for 2 h. After curing, an inert two-part epoxy was mixed and used to cover the back and sides of the monolith as well as the gold paint and approximately 1 inch of the wire to ensure that only the monolith generated an electrochemical response. The inert epoxy was allowed to cure for 12 h.

All electrochemical measurements were conducted using a three-electrode electrochemical cell with 0.1 M $HClO_4$ acid as the supporting electrolyte and a platinum wire as the counter electrode. The applied potential was controlled using a Bio-Logic SP-300 potentiostat while an Ag/AgCl electrode was used as the reference electrode. The reference electrode was placed in a capillary filled with 0.1 M $HClO_4$ acid to further isolate it from the electrolyte and prevent chlorine evolution at high applied potentials. The reference electrode was calibrated against the reversible hydrogen electrode (RHE) scale by measuring the hydrogen evolution/oxidation currents on a polycrystalline Pt disk (Pine) in 0.1 M $HClO_4$ electrolyte and all potentials in this study were referenced to the RHE potential scale.

Capacitance measurements of all monoliths were obtained using CV in an electrolyte saturated with Ar (Airgas, ultra-high purity) prior to measurement by scanning between 0.01 V vs RHE and 1.4 V vs RHE at a series of scan rates between 1 V s^{-1} and 50 mV s^{-1}. The fastest scan rates were measured first, followed by incrementally slower rates. All cyclic voltammograms were measured with iR-compensated potentials to ensure the result reflects the intrinsic electrode response. The total resistance, *R*, was measured using the Biologic automatic software compensation as the AC impedance at high frequency in the three-electrode system and corresponded to the sum of all electrolyte and contact resistances.

3. Results and Discussion

Graded macro- and mesoporous TiO_2 and TiN (Cornell Graded Materials – CGMs) with structural asymmetry along the film normal were obtained using the CNIPS process in combination with a series of thermal processing steps (**Figure 1**). In this study, an ISV triblock terpolymer was employed with a molar mass of 113 kg mol^{-1} with PI, PS, and P4VP volume fractions of 29, 59, and 12 vol%, respectively, and a PDI of 1.3. It was synthesized via a previously reported sequential anionic polymerization process.[17] As demonstrated in earlier studies, incorporating PI as a third block substantially improves the mechanical properties of the as-made membranes, for example, relative to SV diblock copolymer-derived materials, in particular for molar masses below 100 kg mol^{-1} leading to smaller mesopores and therefore higher surface areas.[17,18] In preparation for the CNIPS process, the ISV was dissolved at 15 wt.% in a solvent system of 7:3 (by weight) DOX:THF. The ISV triblock terpolymer was used to structure-direct inorganic TiO_2 sol-gel NPs prepared via a previously reported sol-gel synthesis route, which is expected to selectively swell the hydrophilic P4VP phase.[22,35,36] The TiO_2 sol-gel NPs in THF were added to the homogeneous ISV in DOX:THF solution. The solutions were cast onto glass slides using a doctor blade whose height had been adjusted to 305–381 μm using feeler blades. The solvents in the casted films were allowed to partially evaporate, typically for 75 s, inducing an ISV+TiO_2 concentration gradient along the film normal. Immediately following the set evaporation time, the films were gently plunged into a non-solvent DI water bath. In this step, the polymer precipitates, which freezes-in the structure, converting the concentration gradient into a structural gradient. This concluded the CNIPS part of the process that resulted in organic/inorganic hybrid membranes.

The CNIPS procedure was then followed by a series of thermal processing steps. The films were first dried and then heated to 130 °C to drive off residual solvent or non-solvent. Thereafter, they were either treated at 300, 400, or 500 °C to obtain freestanding oxides (TiO_2) with either some (300 °C), only traces (400 °C), or no (500 °C) remaining carbon, respectively, as suggested by the color in the photographs in Figure 1. These oxides were then

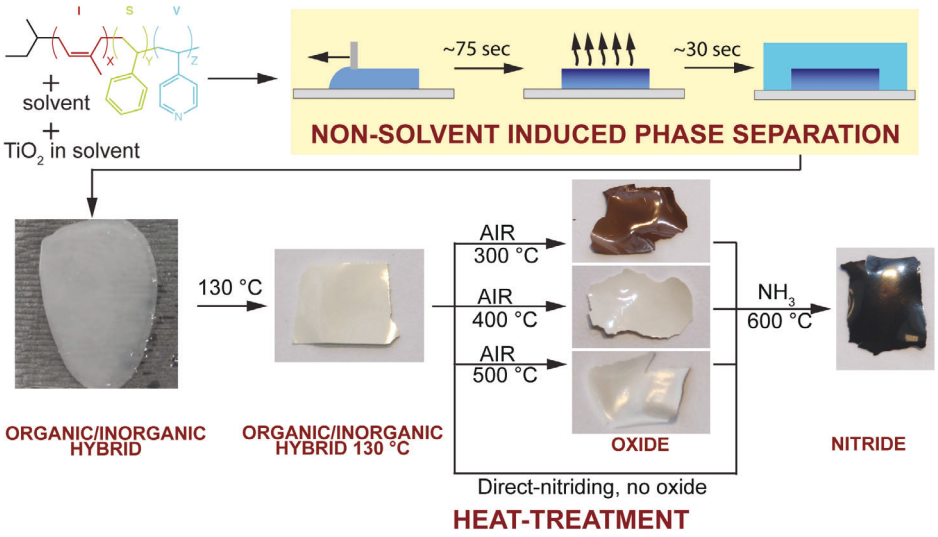

Figure 1. Schematic of the CNIPS process and subsequent thermal processing steps. ISV triblock terpolymer was dissolved in 7:3 (by weight) DOX:THF to which TiO_2 sol NPs in THF were added. The homogeneous casting solution was pipetted onto a glass slide and a film of specified thickness was cast. The solvents were evaporated for a specified amount of time on the order of a minute (see main text) to induce a concentration gradient. Upon immersion into a DI water bath, the polymer was precipitated, converting the ISV+TiO_2 concentration gradient into a structural gradient. The resulting membranes were dried at RT and up to 130 °C in a vacuum oven. They were then subjected to thermal processing steps in a flow furnace that was open to air to either 300, 400, or 500 °C. This led to the decomposition of the polymer and formation of a freestanding oxide. The oxide was then subjected to further heat-treatment in NH_3 (600 °C) to form TiN. In one route, the 130 °C heat-treated hybrid was directly converted in NH_3 (to 600 °C) to the nitride without first being heat processed to the oxide in air. Representative photographs of the materials at each processing step are shown at the bottom (the sample heat-treated in air to only 300 °C appears dark presumably as a result of residual carbon).

treated to 600 °C in flowing NH_3 to obtain freestanding TiN. In one case, the oxide step was omitted by taking the 130 °C hybrid and directly heating it in NH_3 to 600 °C in order to obtain freestanding TiN monoliths.

3.1. Evaporation Time as a Means to Tuning Asymmetric Membrane Substructure

The SNIPS and CNIPS processes depend on a number of input parameters that need to be carefully tuned in order to obtain desired asymmetric membrane structures. Parameters such as composition (either BCP composition in case of SNIPS, or BCP + additive compositions in case of CNIPS), casting solution concentration, casted membrane thickness, or evaporation time all are influencing the final structure, both of the top separation layer as well as of the asymmetric substructure.[20,23,24,37,38] **Figure 2** depicts SEM micrographs of a series of membranes of both the as-made ISV+TiO_2 hybrid materials (Figure 2a) immediately following precipitation and drying as well as the corresponding free-standing oxides, which were all treated to 500 °C (Figure 2b). In this series, the evaporation times varied between 45, 60, 75, and 90 s (from left to right).

From Figure 2a, irrespective of evaporation time the top surfaces (top row) of the as-made materials remained closed. The different images reflect varying degrees of hexagonal order on these top surfaces. With increasing evaporation time, the cross-section evolved from a more finger-like to a more sponge-like profile (middle row, left to right). This transformation has previously been rationalized as resulting from the increased film concentration and thus more viscous solutions at higher evaporation times.[20,39] The higher viscosity delays the solvent and non-solvent exchange, thereby resulting in denser (i.e., more sponge-like) substructures. The bottom surfaces (bottom row) of the membranes only showed small variations. It appears that with increasing evaporation time there were fewer yet larger macropores.

Each of the hybrids in Figure 2a was obtained using different evaporation times followed by conversion into an oxide by treatment in the air using a heating profile of 1 °C min^{-1} to 500 °C with a dwell time of 3 h before being allowed to cool back to RT (Figure 2b). Due to substantial material decomposition, the top surfaces changed from closed to porous (top row). Due to increased contrast in the oxides, the hexagonal pore ordering became particularly evident for evaporation times of 75 and 90 s, respectively. Both the asymmetric cross-sections (middle row) and open bottom surfaces (bottom row) were retained for each respective evaporation time.

Results of XRD experiments on the oxides are provided in Figure S1, Supporting Information. The resulting patterns were consistent with an anatase phase TiO_2 (ICSD #01-070-7348; space group $I4_1/amd$ (#141)) with lattice parameters of a = b = 3.80 Å and c = 9.53 Å, and a coherent scattering domain size of around 15 nm. Analysis results are summarized in Supporting Information Table S1, Supporting Information.

3.2. Thermal Processing of Membranes into Asymmetric Oxides and Nitrides

In general, thermal processing parameters affect material composition and crystallinity, and thus material performance in

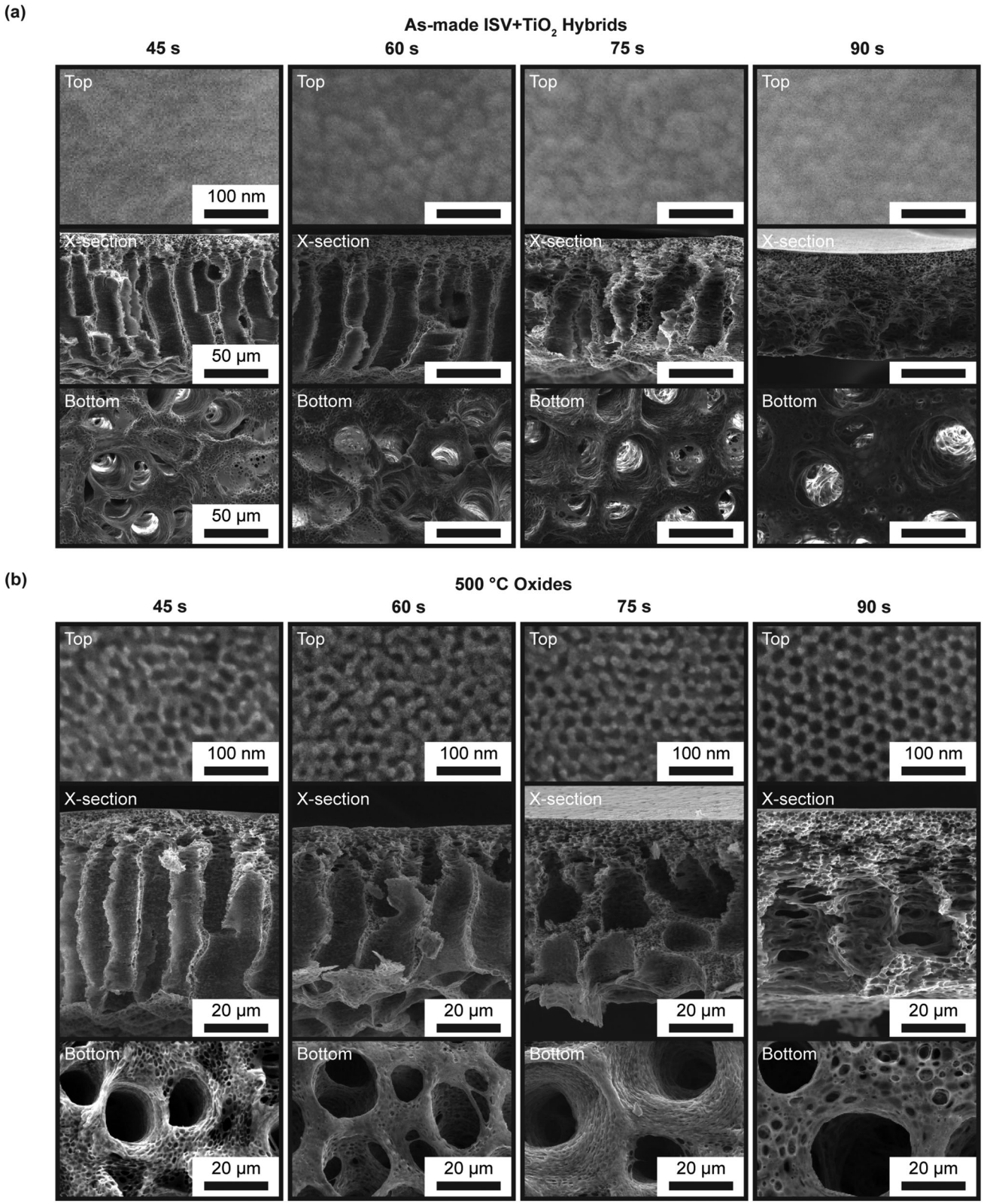

Figure 2. Representative SEM images of asymmetric a) as-made ISV+TiO_2 hybrid membranes and b) TiO_2 materials heated to 500 °C with a dwell time of 3 h before being allowed to cool to RT. From left to right, evaporation times ranged from 45, 60, 75, to 90 s. From top to bottom for both (a) and (b): top surface, asymmetric cross-section, and macroporous bottom surface. Scale bars are identical in each row.

envisioned applications. For example, single-phase TiN may be desirable for electrochemical applications,[25] while mixed-phase materials consisting of crystalline anatase and crystalline TiN may find uses in simultaneous dye-sensitized solar cells (DSSCs) and water-splitting applications.[40]

Here, four pathways were investigated that resulted in either single-phase TiN or mixed-phase anatase TiO_2 and TiN. In particular, the role of oxide crystallinity in the transition from oxide to final nitride was examined. The hybrid precursor membranes in all cases were kept the same. These hybrids were obtained as described above with 75 s evaporation time, drying the as-made ISV+TiO_2 organic/inorganic hybrids (Figure S2, Supporting Information), and then heating them to 130 °C (Figure S3, Supporting Information) in a vacuum oven to drive off any residual solvent (DOX, THF) and non-solvent (DI water). The as-made material top surface was closed (Figure S2a, Supporting Information), yet hexagonal features became evident in the hybrid treated to 130 °C (Figure S3a, Supporting Information). The asymmetric cross-section (Figure S2b, Supporting Information) and open macroporous bottom were evident in both hybrids (Figures S2c and S3c, Supporting Information). The walls of the substructure between macropores at these stages were not porous (Figures S2d and S3d, Supporting Information), a result that was consistent with the closed top surfaces of these hybrids.

Following heat-treatment to 130 °C, subsequent processing pathways were varied. In the first, the ISV+TiO_2 hybrid was directly heated under ammonia to 600 °C to the nitride (Figure 1), bypassing the intermediate oxide formation step. In the other three cases, prior to nitriding, the hybrid was treated to either 300, 400, or 500 °C in air with a dwell time of 3 h before being allowed to cool to RT at ambient rate. This resulted in free-standing asymmetric oxides. Representative SEM images of the 130 °C treated hybrid as well as the various oxides treated to the three different final temperatures are provided in **Figure 3**a–d and Figure S4, Supporting Information. The hybrid treated to 130 °C displayed a top surface with underdeveloped pores (Figure 3a), an asymmetric cross-section with non-porous walls (Figure S4a, Supporting Information), and an open macroporous bottom. When treating the hybrids to either 300 (Figure 3b), 400 (Figure 3c), or 500 °C (Figure 3d), respectively, materials now exhibited more or less hexagonally ordered porous top surfaces while retaining their asymmetric cross-sections and open bottom surfaces (Figure S4b–d, Supporting Information, middle rows). Consistent with the top surface, the walls of the substructure were now also mesoporous due to the decomposition of the polymeric material (Figure S4b–d, Supporting Information, bottom row), thereby adding another layer of pore hierarchy to the materials.

The nitriding step for all the materials was kept the same by heating at 5 °C min^{-1} to 600 °C with a dwell time of 6 h under flowing NH_3. Representative SEM images of the resulting materials are provided in Figure 3e–h. The nitrides retained the main features that were already evident in the case of the oxides, including the porous top surface morphology, the asymmetric cross-sections with additional mesopores in the walls between macropores, as well as the bottom surfaces with large and open macropores. Even though the SEM images of the various nitrides appeared similar, XRD patterns indicated differences resulting from variations in the temperature processing conditions (**Figure 4**, **Table 1**). All materials were derived from ISV+TiO_2 hybrids treated to 130 °C, which were amorphous (Figure 4, black bottom trace). When converting the 130 °C treated hybrid directly to TiN in NH_3, that is, without the intermediate oxide formation step (Figure 1), the material underwent an amorphous to crystalline transition. The resulting crystalline nitride had peaks consistent with a cubic rocksalt TiN (ICSD entry #00-038-1420; space group $Fm\bar{3}m$ (#225)). The associated lattice parameter was 4.21 Å and the coherent scattering domain size, determined from a Debye–Scherrer analysis (Experimental Section), was 5.7 nm.

The oxide treated to 300 °C in air displayed weak peaks in XRD patterns, relative to all other oxide samples (vide infra), that were consistent with anatase TiO_2 (ICSD #01-070-7348; space group $I4_1/amd$ (#141)) with lattice parameters of a = b = 3.80 Å and c = 9.55 Å, and a coherent scattering domain size of around 11 nm (Experimental Section). When subsequently subjected to thermal processing under NH_3 to 600 °C, in XRD patterns the oxide peaks disappeared and TiN peaks emerged that were consistent with cubic rocksalt TiN with a lattice parameter of 4.22 Å and a coherent scattering domain size of 6.1 nm, consistent with a crystal-to-crystal transition. The dark color of the resulting samples (Figure 1) suggested some residual carbon and/or oxygen in the nitride lattice (vide infra).

The oxide treated to the highest temperature of 500 °C in air displayed peaks in XRD consistent with anatase TiO_2, with lattice parameters of a = b = 3.80 Å and c = 9.54 Å, and a coherent scattering domain size of around 12 nm. When further thermally processed in NH_3 to 600 °C, XRD peaks consistent with both anatase TiO_2 and TiN were observed. The anatase TiO_2 had lattice parameters of a = b = 3.80 Å and c = 9.55 Å, and a substantially increased coherent scattering domain size of around 23 nm. The remaining peaks were consistent with a cubic rocksalt TiN structure with a lattice parameter of 4.21 Å and a coherent scattering domain size of 7.4 nm. In contrast to the results obtained for the lower temperature anneal in air to 300 °C, these data suggested an incomplete crystal-to-crystal transition. The intermediate oxide material appeared white to the eye (Figure 1), consistent with no substantial residual carbon (see also TGA results in Figure S5, Supporting Information). The mixed crystallinity of the final material may pose issues in certain applications, for example, due to reduced conductivity of the mixed TiO_2/TiN composition relative to pure TiN.

In an effort to develop a thermal processing protocol to asymmetric TiN removing all carbon prior to nitriding and no remaining crystalline oxide peaks in the final material, we tested hybrids heat-treated in air to 400 °C before further thermal processing under NH_3 to 600 °C. Interestingly, for this thermal history, two results were obtained—which we will call samples 1 and 2. In sample 1, the oxide exhibited crystalline peaks again consistent with anatase TiO_2 with lattice parameters of a = b = 3.80 Å and c = 9.54 Å, and a coherent scattering domain size of around 14 nm. The final nitride peaks were again consistent with cubic rocksalt TiN with a lattice parameter of 4.21 Å and a coherent scattering domain size of 7.2 nm. In this sample the full crystal-to-crystal transition from oxide to nitride was successful. Another sample (sample 2) that was also treated to 400 °C resulted in an oxide with similar crystallinity consistent with anatase TiO_2 and a coherent scattering domain size of around 13.0 nm. Yet the final nitride still showed some residual crystalline oxide phase in addition to the dominant crystalline nitride phase. The associated

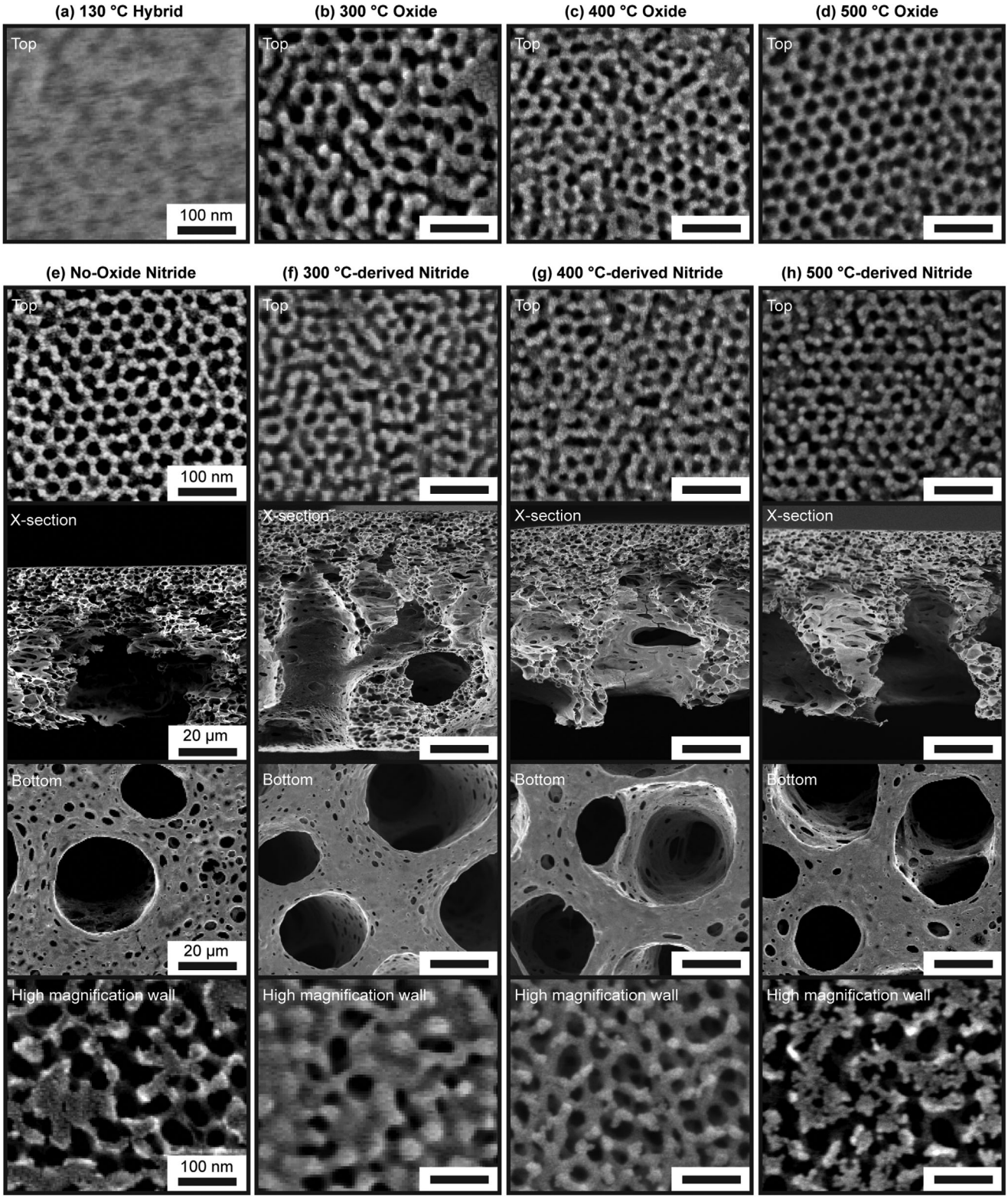

Figure 3. Representative SEM images of asymmetric oxides and nitrides obtained from different thermal processing protocols. Top row: Representative top surface SEM images of a) 130 °C organic/inorganic hybrid, as well as oxides treated in air to b) 300, c) 400, and d) 500 °C, respectively. Rows two to five: Representative SEM images of nitrides resulting from thermal processing in ammonia up to 600 °C obtained e) directly from 130 °C treated hybrid, as well as from oxides heat treated in air to f) 300, g) 400, and h) 500 °C, respectively. Rows two to five show top surfaces, cross-sections, bottom surfaces, and images of the wall between macropores in the substructure, respectively. All oxides and nitrides were made from hybrids evaporated for 75 s. Scale bars are identical in each row.

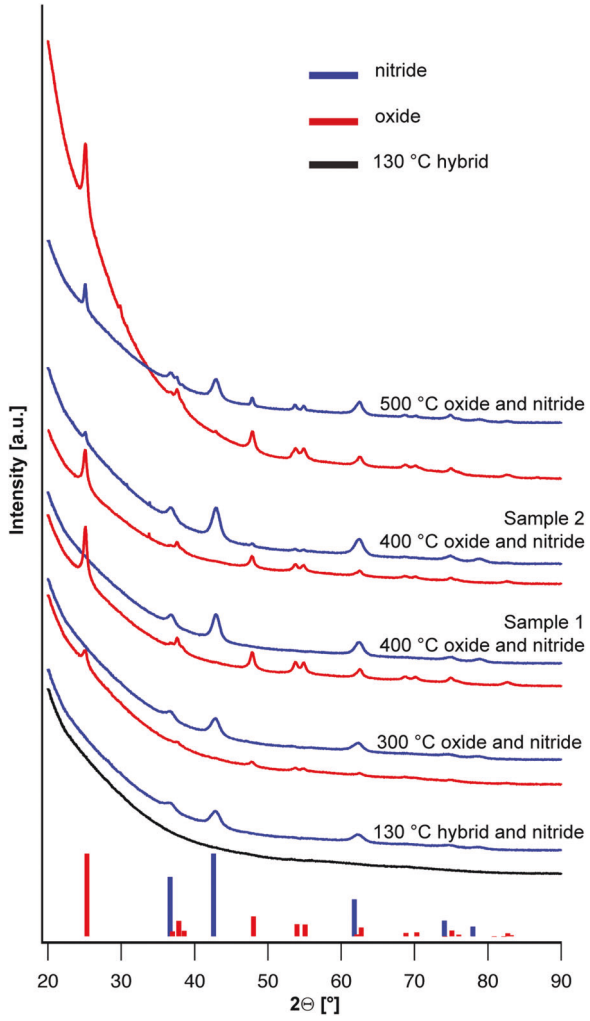

Figure 4. XRD of asymmetric materials obtained from the four pathways to TiN (blue) and their corresponding precursors (hybrid in black, oxides in red). Red tick marks correspond to the expected peak positions and relative intensities of a tetragonal crystal system of anatase TiO_2 ($I4_1/amd$, space group #141, ICSD #01-070-7348). Blue tick marks correspond to the expected peak positions and relative intensities for cubic TiN ($Fm\bar{3}m$, space group #225, ICSD #00-038-1420).

oxide peaks were consistent with anatase TiO_2 and a much increased coherent scattering domain size of around 19 nm. The remaining peaks were consistent with cubic rocksalt TiN with a lattice parameter of 4.21 Å and a coherent scattering domain size of 6.7 nm. At a maximum oxide processing temperature of 400 °C, one sample was transformed to a nitride, while the other retained some crystalline oxide. We hypothesize that this difference might be due to slight variations in sample location within the furnace tube leading to slight variations in processing temperature. Overall, results from XRD suggested that in order to obtain phase pure asymmetric TiN one may use two routes. The first and simplest route involves preheating the polymer-sol hybrid sample at 130 °C and then immediately subjecting the sample to thermal processing under NH_3 up to 600 °C. The second route involves first generating a porous oxide by taking the 130 °C treated hybrid to temperatures around 400 °C before conversion to the nitride.

In addition to structural characterization via XRD, the porosity and surface area of the various materials were investigated via nitrogen sorption/desorption measurements. Results are summarized in **Table 2**, while the corresponding nitrogen sorption/desorption isotherms and pore size distribution graphs derived therefrom for oxides and nitrides are provided in Figures S6 and S7, Supporting Information, respectively (see also Experimental Section). When comparing materials characteristics of the oxide materials in Table 2, BET surface areas were between 40 and 60 $m^2\ g^{-1}$, with the pore size decreasing with increased processing temperature from 49 to 42 to 37 nm for the oxides derived from processing at 300, 400, and 500 °C, respectively. This decrease in pore size was likely correlated with the increased anatase crystal size as a function of increasing processing temperature (Table 1). Overall, measured characteristics were in line with literature values reported for mesoporous TiO_2.[13,41]

In the case of the nitrides, nitrogen sorption/desorption measurements were only performed on single-phase materials, that is, on nitrides either derived from oxides processed at 300 and 400 °C, or directly derived from hybrids taken to 130 °C only before conversion to a nitride (Figure 1). BET surface areas were higher than for the oxides, likely due to the lower mass of the nitrides relative to the oxides as well as their higher density, and varied between 90 and 178 $m^2\ g^{-1}$. The trend in pore size followed that for the oxides with marginal differences between the two series.

Table 1. Summary of XRD-derived structural characteristics of asymmetric oxides and nitrides. Lattice constants (LC), a and c, for anatase, the crystal size (XS) for anatase, the LC, a, for nitrides, and the crystal size (XS) for nitrides are provided.

Sample	Anatase LC a [Å]	Anatase LC c [Å]	Anatase XS [nm]	Nitride LC a [Å]	Nitride XS [nm]
Nitride derived from 500 °C-oxide	3.80	9.55	23	4.21	7.4
500 °C oxide	3.80	9.54	12	–	–
Nitride derived from 400 °C-oxide sample 2	3.80	9.56	19	4.21	6.7
400 °C oxide sample 2	3.80	9.54	13	–	–
Nitride derived from 400 °C-oxide sample 1	–	–	–	4.21	7.2
400 °C oxide sample 1	3.80	9.54	14	–	–
Nitride derived from 300 °C-oxide	–	–	–	4.22	6.1
300 °C oxide	3.80	9.55	11	–	–
Nitride no oxide	–	–	–	4.21	5.7
130 °C hybrid	–	–	–	–	–

Table 2. Nitrogen sorption/desorption derived materials characteristics of asymmetric oxides and nitrides.

Sample	BET surface area [$m^2\ g^{-1}$]	Micropore surface area [$m^2\ g^{-1}$]	Peak pore size [nm]	FWHM [nm]	Single point adsorption pore volume [$cm^3\ g^{-1}$]
500 °C oxide	43 ± 4.3	18	37	19 ± 8.3	0.43
Nitride derived from 400 °C-oxide	90 ± 3.0	15	41	17 ± 7.1	0.59
400 °C oxide	60 ± 1.1	11	42	16 ± 6.8	0.57
Nitride derived from 300 °C-oxide	178 ± 19	56	38	17 ± 7.1	0.54
300 °C oxide	57 ± 1.7	26	49	22 ± 9.5	0.49
Nitride no oxide	105 ± 6.0	28	50	18 ± 7.8	0.80

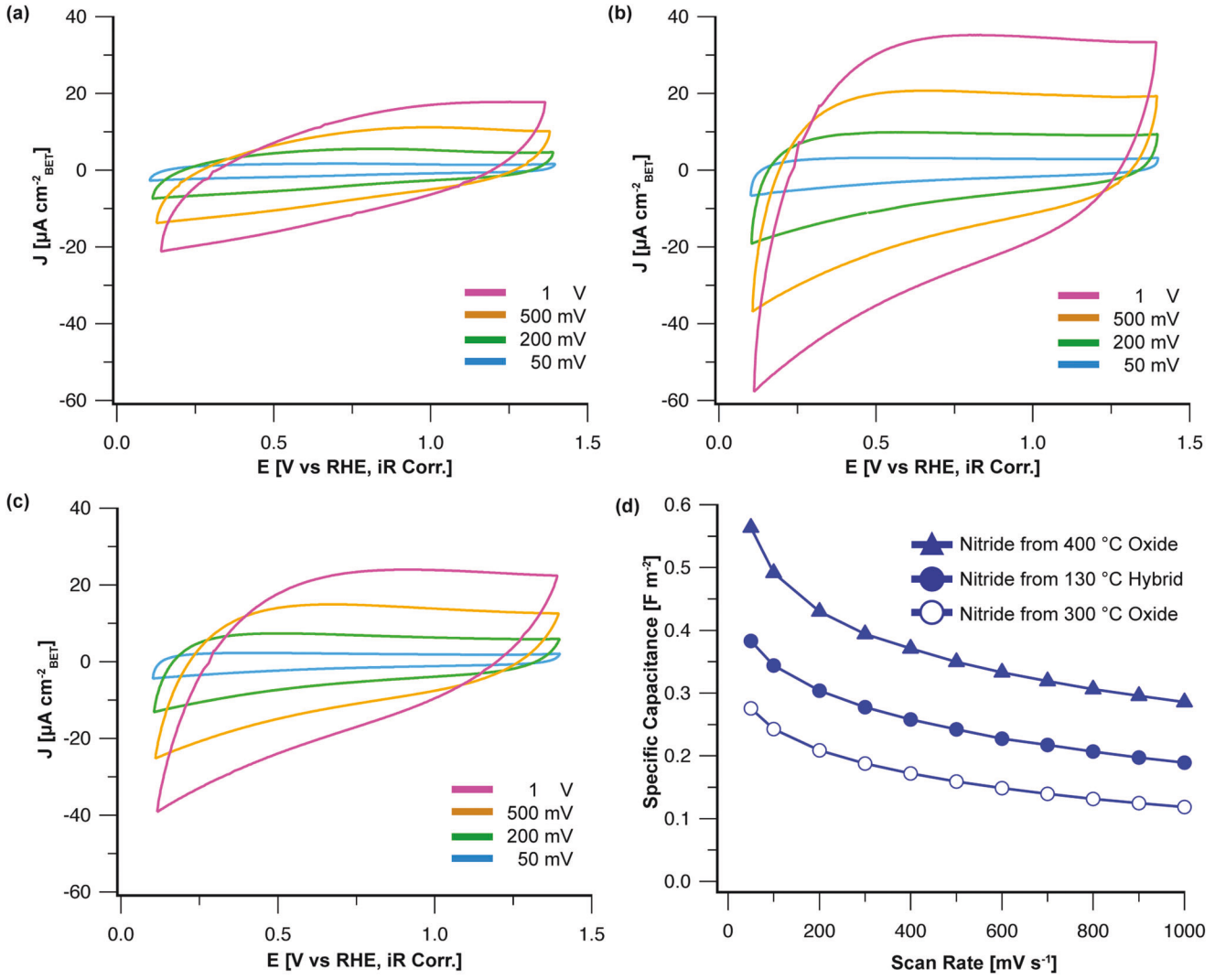

Figure 5. Electrochemical characterization of phase-pure asymmetric and hierarchically porous TiN samples. Cyclic voltammograms for phase-pure TiN monoliths derived from oxides heat-treated to a) 300 and b) 400 °C, or directly from hybrids processed to only c) 130 °C. Scan rates shown include: 50 mV s^{-1} (blue), 200 mV s^{-1} (green), 500 mV s^{-1} (orange), and 1 V s^{-1} (pink). d) Scan rate dependence of specific capacitance for the three asymmetric TiN samples in (a) to (c) showing improved specific capacitance with more complete polymer removal. All results were collected in Ar-saturated 0.1 M $HClO_4$.

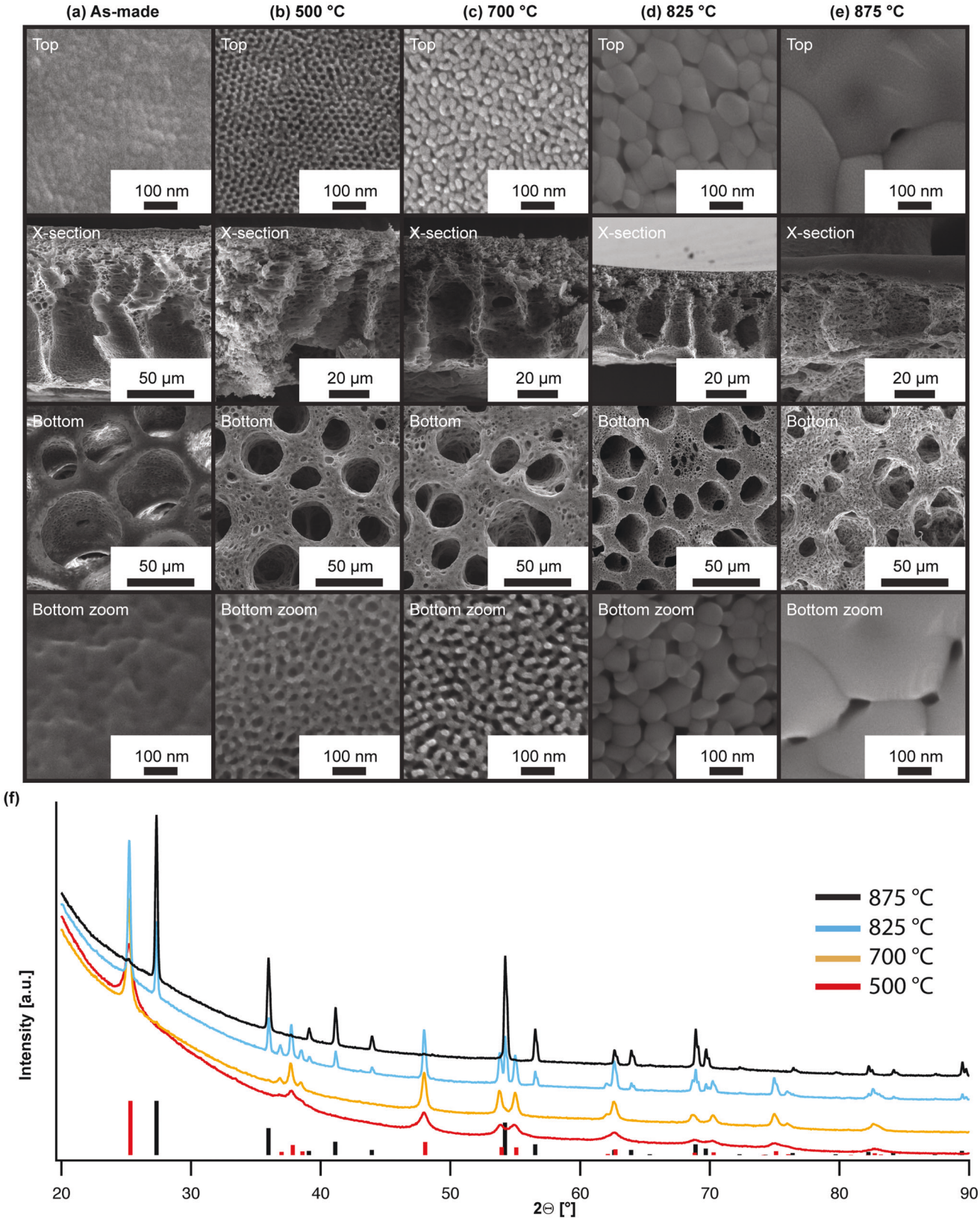

Figure 6. Characterization of asymmetric oxide materials treated to different temperatures. Representative SEM images of asymmetric a) parent as-made hybrid material and b–e) resulting TiO_2 membranes from materials shown in (a) heated in air to (b) 500, (c) 700, (d) 825, and (e) 875 °C. From

3.3. Electrochemical Characterization of Single-Phase Asymmetric TiN

In an earlier study, we demonstrated that asymmetric TiN with polymer removal conducted at 400 °C under air to form an oxide before conversion to the nitride led to state-of-the-art power density at competitive energy density when used as an EDLC electrode.[15] To characterize the effects of thermal processing on the capacitive performance, CV in 0.1 M $HClO_4$ at a series of scan rates between 50 mV s^{-1} and 1 V s^{-1} was used with each of the phase-pure nitrides (**Figure 5**a–c, Figure S8a,b, Supporting Information). Specific and gravimetric capacitance was calculated for each material at all scan rates as well as the retention of the 50 mV s^{-1} capacitance at 1 V s^{-1} (Figure 5d, Figure S8c,d, Supporting Information). The specific capacitance shown in Figure 5d monotonically decreased with the scan rate for all samples measured due to mass transport limitation. This decrease is present even in the highly accessible asymmetric structures and is an indicator of the accessibility of the nitrides. Among the samples tested, the TiN electrode obtained from an intermediate oxide formation step at 400 °C had the highest specific capacitance for all scan rates tested, followed by the sample directly converted into the nitride without intermediate oxide formation step and finally the sample heat-treated to 300 °C in the intermediate oxide formation step (compare areas enclosed by scans in Figure 5a–c). Interestingly, this behavior was inversely correlated with BET surface area, which increased in the same sequence from 90 ± 3.0 (nitride derived from 400 °C-treated oxide) to 105 ± 6.0 (130 °C-hybrid-derived nitride) to 178 ± 19 m^2 g^{-1} (nitride derived from 300 °C-treated oxide). This trend suggests that the nitride samples derived from 400 °C-treated oxide had a greater degree of microporosity but the pores were inaccessible at fast rates. When treated at higher temperature, the surface area decreases but the pores become more accessible to positively affect the capacitance.

3.4. Anatase to Rutile Transition in Asymmetric TiO_2 Membranes

Mixed-phase oxides such as TiO_2 consisting of both anatase and rutile have potential applications in photocatalysis.[42,43] By changing the thermal processing conditions used to generate the intermediate oxide, the structure and crystal phase of the materials could be tuned as evidenced by SEM and XRD data analysis (**Figure 6**, **Table 3**). From top to bottom, rows in Figure 6 show SEM images of top surfaces, cross sections, and bottom surfaces, as well as of mesoporous walls between macropores in the substructure for oxides submitted to different thermal processing conditions. The as-made hybrid (Figure 6a) used to generate all these oxide materials was asymmetric with a hexagonally structured top surface atop a macroporous substructure. After thermal processing to 500 °C in air, XRD peaks (Figure 6f) were consistent with anatase TiO_2 with lattice parameters of a = b = 3.79 Å and c = 9.52 Å, and a coherent scattering domain size of around 12 nm. In a material heated to 700 °C, while the lattice parameters remained similar, the coherent scattering domain size increased to about 26 nm. The increased crystal size was also evident from SEM, see in particular the top surface image in Figure 6c now showing a disordered pore structure and struts with sizes thicker than those depicted for the sample treated to only 500 °C.

When processed to higher temperatures of 825 or 875 °C (Figure 6d,e), overall asymmetric membrane structure with hierarchical porosity (i.e., meso- and macroporosity) was retained, but now SEM images of top surfaces and walls between macropores in the substructure showed polycrystalline structures with substantially increased crystal sizes. This is particularly true for the highest processing temperature of 875 °C tested. Furthermore, XRD data of these materials suggested that in addition to anatase TiO_2 a second phase developed, that is, rutile TiO_2 (Figure 6f). This was expected as typically in synthetic titania, the anatase to rutile transition temperature lies between 600 and 700 °C.[13,44–46] In fact, at 825 °C (Figure 6d) substantial crystal overgrowth was already evident in SEM images of top surface and substructure walls. Furthermore, XRD data analysis now suggested a mixed-phase material with peaks consistent with anatase TiO_2 with lattice parameters of a = b = 3.79 Å and c = 9.53 Å, and a coherent scattering domain size of around 37 nm, as well as rutile TiO_2 (ICSD #00-021-1276; space group $P4_2/mnm$ (#136)) with lattice parameters of a = b = 4.60 Å and c = 2.97 Å, and a coherent scattering domain size of around 52 nm. The even higher processing temperature of 875 °C resulted in even stronger crystal overgrowth (Figure 6e). At this temperature, the anatase to rutile transition seemed complete with unchanged rutile lattice parameters of a = b = 4.60 Å and c = 2.97 Å, and a coherent scattering domain size of around 43 nm.

4. Conclusion

We have demonstrated the synthesis of porous inorganic membrane materials exhibiting a combination of asymmetric pore structure along the film normal with well-defined mesoporosity throughout the materials by utilizing a combination of BCP co-assembly with sol-gel derived TiO_2 sol NPs and non-solvent induced phase separation (C+NIPS = CNIPS). Tuning CNIPS and subsequent thermal processing parameters have led to asymmetric oxides and nitrides with tailored properties. By changing the evaporation time in the CNIPS procedure, various membrane cross-sections, from more finger-like to more sponge-like, could be obtained. In the membrane field, changes in substructure are expected to determine mechanical properties,[20] while in electrochemical storage and conversion devices such changes can influence the electrochemical response, for example, ion diffusion rates.[15] Varying thermal processing conditions, material composition, crystallinity, and porosity could be tuned, both in the oxides as well as in the resulting nitrides. For example, by increasing the processing temperature of the hybrids and oxides in

top to bottom, rows of images depict top surfaces, asymmetric cross-sections, bottom surfaces, and substructure walls between macropores. f) Powder XRD of asymmetric oxides from various processing temperatures (from bottom to top): 500 (red), 700 (orange), 825 (blue), and 875 °C (black). Red tick marks correspond to the expected peak positions and relative intensities of a tetragonal crystal system of anatase TiO_2 ($I4_1/amd$, space group #141, ICSD #01-070-7348). Black tick marks correspond to the expected peak positions and relative intensities of a tetragonal crystal system of rutile TiO_2 ($P4_2/mnm$, space group #136, ICSD #00-021-1276).

Table 3. Summary of XRD-derived characteristics of asymmetric oxides.

Temperature [°C]	Anatase LC a [Å]	Anatase LC c [Å]	Anatase XS [nm]	Rutile LC a [Å]	Rutile LC c [Å]	Rutile XS [nm]
875	–	–	–	4.60	2.97	43
825	3.79	9.53	37	4.60	2.97	52
700	3.79	9.53	26	–	–	–
500	3.79	9.52	12	–	–	–

air, the final crystal structure could be controlled from phase-pure anatase TiO_2 to phase-pure rutile TiO_2, with mixed-phase materials at intermediate temperatures. Increasing the processing temperature of the hybrid or intermediate oxide materials before the nitriding step in NH_3 allowed switching from mixed-phase oxide/nitride materials to single-phase nitrides. We further probed the effects of the thermal processing conditions on the use of asymmetric phase-pure TiN as an EDLC electrode using CV and found that they influence, for example, specific capacitance. We expect that such structure-property correlations will provide insights into how to further improve asymmetric materials performance in applications including electrochemical energy storage and conversion. Furthermore, we hope that improving our fundamental understanding of details of the inorganic asymmetric membrane formation mechanisms will allow the CNIPS process to be expanded to other inorganic materials classes, including catalytically active materials.

Supporting Information

Supporting Information is available from the Wiley Online Library or from the author.

Acknowledgements

This work was funded by the National Science Foundation under award DMR-1707836. J.S. acknowledges support from the Center for Alkaline-Based Energy Solutions (CABES), an Energy Frontier Research Center funded by the U.S. Department of Energy, Office of Science, Office of Basic Energy Sciences, under Award No. DE-SC0019445 (electrochemical characterization). This work made use of the Cornell Center for Materials Research Shared Facilities which were supported through the NSF MRSEC program (DMR-1719875). P.A.B. was supported by the National Science Foundation Graduate Research Fellowship Program (DGE-1650441).

Author Contributions

S.A.H., P.A.B., and U.W. conceived the project. S.A.H. performed the materials synthesis and characterization and analysis via SEM, XRD, and nitrogen sorption. K.E.F. performed and analyzed the electrochemical measurements under the supervision of J.S. F.J.D., P.A.B., and E.M.S. assisted in XRD characterization. S.A.H. and U.W. wrote the manuscript with assistance from K.E.F. and input from all co-authors.

Conflict of Interest

The authors declare that they have submitted a patent disclosure based on this study through Cornell University.

Data Availability Statement

The data that support the findings of this study are available from the corresponding author upon reasonable request.

Keywords

asymmetric structure, porous, sol gel, titanium nitride, titanium oxide

Received: August 20, 2022
Revised: September 26, 2022
Published online: October 25, 2022

[1] P. Simon, Y. Gogotsi, B. Dunn, *Science* **2014**, *343*, 1210.
[2] Y. Gogotsi, P. Simon, *Science* **2011**, *334*, 917.
[3] D. R. Rolison, J. W. Long, J. C. Lytle, A. E. Fischer, C. P. Rhodes, T. M. McEvoy, M. E. Bourg, A. M. Lubers, *Chem. Soc. Rev.* **2009**, *38*, 226.
[4] J. W. Long, B. Dunn, D. R. Rolison, H. S. White, *Chem. Rev.* **2004**, *104*, 4463.
[5] A. S. Aricò, P. G. Bruce, B. Scrosati, J. - M. Tarascon, W. Van Schalkwijk, *Nat. Mater.* **2005**, *4*, 366.
[6] S. Martinet, in *Nanomaterials for Sustainable Energy. NanoScience and Technology*, Springer, Cham **2016**, pp. 471–512.
[7] Y. Sun, N. Liu, Y. Cui, *Nat. Energy* **2016**, *1*, 16071.
[8] J. G. Werner, G. G. Rodríguez-Calero, H. D. Abruña, U. Block Wiesner, *Energy Environ. Sci.* **2018**, *11*, 1261.
[9] T. Lin, I. W. Chen, F. Liu, C. Yang, H. Bi, F. Xu, F. Huang, *Science* **2015**, *350*, 1508.
[10] M. C. Orilall, U. Wiesner, *Chem. Soc. Rev.* **2011**, *40*, 520.
[11] D. Zhao, J. Feng, Q. Huo, N. Melosh, G. H. G. Fredrickson, B. F. B. Chmelka, G. D. G. Stucky, *Science* **1998**, *279*, 548.
[12] J. G. Werner, T. N. Hoheisel, U. Wiesner, *ACS Nano* **2014**, *8*, 731.
[13] J. Lee, M. Christopher Orilall, S. C. Warren, M. Kamperman, F. J. DiSalvo, U. Wiesner, *Nat. Mater.* **2008**, *7*, 222.
[14] J. G. Werner, S. S. Johnson, V. Vijay, U. Wiesner, *Chem. Mater.* **2015**, *27*, 3349.
[15] S. A. Hesse, K. E. Fritz, P. A. Beaucage, R. P. Thedford, F. Yu, F. J. DiSalvo, J. Suntivich, U. Wiesner, *ACS Nano* **2020**, *14*, 16897.
[16] K. V. Peinemann, V. Abetz, P. F. W. Simon, *Nat. Mater.* **2007**, *6*, 992.
[17] W. A. Phillip, R. M. Dorin, J. Werner, E. M. V Hoek, U. Wiesner, M. Elimelech, *Nano Lett.* **2011**, *11*, 2892.
[18] R. M. Dorin, H. Sai, U. Wiesner, *Chem. Mater.* **2014**, *26*, 339.
[19] X. Qiu, H. Yu, M. Karunakaran, N. Pradeep, S. P. Nunes, K. V. Peinemann, *ACS Nano* **2013**, *7*, 768.
[20] Q. Zhang, Y. M. Li, Y. Gu, R. M. Dorin, U. Wiesner, *Polymer* **2016**, *107*, 398.
[21] M. M. Pendergast, R. Mika Dorin, W. A. Phillip, U. Wiesner, E. M. V. Hoek, *J. Membr. Sci.* **2013**, *444*, 461.
[22] Y. Gu, R. M. Dorin, U. Wiesner, *Nano Lett.* **2013**, *13*, 5323.
[23] S. A. Hesse, J. G. Werner, U. Wiesner, *ACS Macro Lett.* **2015**, *4*, 477.

[24] S. A. Hesse, P. A. Beaucage, D. M. Smilgies, U. Wiesner, *Macromolecules* **2021**, *54*, 2979.
[25] K. E. Fritz, P. A. Beaucage, F. Matsuoka, U. Wiesner, J. Suntivich, *Chem. Commun.* **2017**, *53*, 7250.
[26] Y. Wu, Z. Liu, F. Ran, *Microporous Mesoporous Mater.* **2019**, *275*, 14.
[27] X. Yang, Y. Chen, M. Wang, H. Zhang, X. Li, H. Zhang, *Adv. Funct. Mater.* **2016**, *26*, 8427.
[28] F. Ran, K. Shen, Y. Tan, B. Peng, S. Chen, W. Zhang, X. Niu, L. Kong, L. Kang, *J. Membr. Sci.* **2016**, *514*, 366.
[29] M. Stefik, S. Wang, R. Hovden, H. Sai, M. W. Tate, D. A. Muller, U. Steiner, S. M. Gruner, U. Wiesner, *J. Mater. Chem.* **2012**, *22*, 1078.
[30] S. W. Robbins, H. Sai, F. J. DiSalvo, S. M. Gruner, U. Wiesner, *ACS Nano* **2014**, *8*, 8217.
[31] S. W. Robbins, P. A. Beaucage, H. Sai, K. W. Tan, J. G. Werner, J. P. Sethna, F. J. DiSalvo, S. M. Gruner, R. B. Van Dover, U. Wiesner, *Sci. Adv.* **2016**, *2*, e1501119.
[32] S. Brunauer, P. H. Emmett, E. Teller, *J. Am. Chem. Soc.* **1938**, *60*, 309.
[33] K. S. W. Sing, D. H. Everett, R. A. W. Haul, L. Moscou, R. A. Pierotti, J. Rouquérol, T. Siemieniewska, *Pure Appl. Chem.* **1985**, *57*, 603.
[34] E. P. Barrett, L. G. Joyner, P. P. Halenda, *J. Am. Chem. Soc.* **1951**, *73*, 373.
[35] C. C. Weng, K. F. Hsu, K. H. Wei, *Chem. Mater.* **2004**, *16*, 4080.
[36] Q. Lou, P. S. Chinthamanipeta, D. A. Shipp, *Langmuir* **2011**, *27*, 15206.
[37] Y. M. Li, Q. Zhang, J. R. Álvarez-Palacio, I. F. Hakem, Y. Gu, M. R. Bockstaller, U. Wiesner, *Polymer* **2017**, *126*, 368.
[38] M. Müller, V. Abetz, *Chem. Rev.* **2021**, *121*, 14189.
[39] A. K. Hołda, B. Aernouts, W. Saeys, I. F. J. Vankelecom, *J. Membr. Sci.* **2013**, *442*, 196.
[40] C. T. Li, S. R. Li, L. Y. Chang, C. P. Lee, P. Y. Chen, S. S. Sun, J. J. Lin, R. Vittal, K. C. Ho, *J. Mater. Chem. A* **2015**, *3*, 4695.
[41] P. Docampo, S. Guldin, M. Stefik, P. Tiwana, M. C. Orilall, S. Hüttner, H. Sai, U. Wiesner, U. Steiner, H. J. Snaith, *Adv. Funct. Mater.* **2010**, *20*, 1787.
[42] D. C. Hurum, A. G. Agrios, K. A. Gray, T. Rajh, M. C. Thurnauer, *J. Phys. Chem. B* **2003**, *107*, 4545.
[43] Z. Luo, A. S. Poyraz, C. H. Kuo, R. Miao, Y. Meng, S. Y. Chen, T. Jiang, C. Wenos, S. L. Suib, *Chem. Mater.* **2015**, *27*, 6.
[44] M. K. Seery, R. George, P. Floris, S. C. Pillai, *J. Photochem. Photobiol., A* **2007**, *189*, 258.
[45] S. C. Padmanabhan, S. C. Pillai, J. Colreavy, S. Balakrishnan, D. E. McCormack, T. S. Perova, Y. Gun'ko, S. J. Hinder, J. M. Kellys, *Chem. Mater.* **2007**, *19*, 4474.
[46] C. P. Kumar, N. O. Gopal, T. C. Wang, M. S. Wong, S. C. Ke, *J. Phys. Chem. B* **2006**, *110*, 5223.